Journal of Geophysical Research: Solid Earth

RESEARCH ARTICLE
10.1029/2017JB014613

Special Section:
Seismic and Micro-Seismic Signature of Fluids in Rocks: Bridging the Scale Gap

Microseismic Emissions During Pneumatic Fracturing: A Numerical Model to Explain the Experiments

Antoine L. Turquet[1], Renaud Toussaint[1], Fredrik Kvalheim Eriksen[1,2], Guillaume Daniel[3], Daniel Koehn[4], and Eirik G. Flekkøy[2]

[1]Université de Strasbourg, CNRS, Institut de Physique du Globe de Strasbourg, UMR7516, Strasbourg, France, [2]PoreLab, The Njord Centre, Department of Physics, University of Oslo, Oslo, Norway, [3]Magnitude, Sainte-Tulle, France, [4]School of Geographical and Earth Sciences, University of Glasgow, Glasgow, UK

Abstract Modeling of fluid injection processes into a deformable porous medium is a challenging area of physics that has a wide range of applications like the food, construction, and petroleum industries. In this research, we investigate pneumatic fracturing of a porous medium experimentally and numerically in a Hele-Shaw cell. In the experiments, we inject air into the porous medium (initially random loose packed) to create compaction, channeling, and fracturing while monitoring the cell with accelerometers and a high-speed camera. Furthermore, we develop a numerical model in two steps: (1) a poroelastoplasticity-based model to explain dynamic fluid pressure variations and (2) a solid stress model based on Janssen's theory. The contributions of the different pressure sources air in channels and solid stress in the experiments, and the simulations are compared with respect to amplitude and frequency. Afterward, the variations of the normal stress exerting on the plates are convolved with a Lamb Wave green function to generate acoustic emissions numerically. The physics behind the evolution of the experimentally recorded power spectrum of the out-of-plane plate vibrations are explained using numerical models. The frequency bands (in the simulated power spectra) are influenced by the size of the opened channels and the Hele-Shaw cell and are in the same range with the experimentally measured peaks of the acoustic emissions.

Key Points:
- A transparent experimental model of air injection into a porous medium is monitored using a high-speed camera and accelerometers
- A numerical model explaining the solid-fluid-coupled mechanics is generated to explain the experimental results further
- Solid-fluid interactions generate acoustic signals possessing similar microseismic patterns as those observed by the accelerometers

Supporting Information:
- Supporting Information S1
- Movie S1
- Movie S2
- Movie S3

Correspondence to:
A. L. Turquet,
turquetal@gmail.com

Citation:
Turquet, A. L., Toussaint, R., Eriksen, F. K., Daniel, G., Koehn, D., & Flekkøy, E. G. (2018). Microseismic emissions during pneumatic fracturing: A numerical model to explain the experiments. *Journal of Geophysical Research: Solid Earth*, *123*, 6922–6939. https://doi.org/10.1029/2017JB014613

Received 30 JUN 2017
Accepted 10 JUL 2018
Accepted article online 16 JUL 2018
Published online 31 AUG 2018

1. Introduction

Fluid flow inside granular media is a very common phenomenon in nature and in industrial applications. Particularly, if the fluid flow is pressurized, it can induce rapid porosity changes inside the porous medium which is in contact with the fluid, like fracturing and channeling (Benson et al., 2008; Bouchut et al., 2016; J. A. Eriksen, Toussaint, et al., 2015; Farquharson et al., 2016, 2015; Galland et al., 2018; Gidaspow, 1994; Goren et al., 2010, 2011; Johnsen, Chevalier, et al., 2008; Johnsen et al., 2006; Johnsen, Toussaint, et al., 2008; Kunii & Levenspiel, 1991; Trulsson et al., 2012; Vinningland et al., 2007a, 2007b, 2010, 2012). This type of brittle deformation is visible in nature (e.g., volcanic activities and tremors), and in engineering (ground improvements, CO_2 sequestration, and fracturing applications; Agency, 1994; Aochi et al., 2011; Charléty et al., 2007; Cuenot et al., 2008; Dorbath et al., 2009; Gao et al., 2014; Schuring et al., 1996). Deformations based on momentum exchange between the nonmiscible solid and fluid phases can lead to different characteristic shapes and structures of deformation (bubbles, J. A. Eriksen, Marks, et al., 2015; J. A. Eriksen, Toussaint et al., 2015; J. A. Eriksen, et al., 2018; Holtzman et al., 2012; McNamara et al., 2000; fractures, Flekkøy et al., 2002; Ghani et al., 2015, 2013; Šílený et al., 2009; Vass et al., 2014; and channels, Abdelmalak et al., 2012; Hurst et al., 2011; Jamtveit et al., 2004; Lemaire et al., 1993; Svensen et al., 2006). These shapes change depending on the characteristics of the solid (e.g., density, particle size, and permeability) and the fluid (e.g., viscosity and compressibility) and boundary conditions (e.g., applied pressure, shape and permeability of the boundaries, gravity orientation, and loading rate). Microseismic monitoring is a routine protocol during well operations in the industry, but interpretation of this data is an applied research topic (Cornet, 2015; Cornet et al., 1998; Valkó & Economides, 1995) in which there are still questions to be answered. For example, Elkhoury et al. (2006) studied the relationship of permeability with seismicity in Southern California and has shown that permeability can increase up to 3 times depending on the peak ground velocity of the earthquake. Next, Benson et al. (2010) studied seismic events in volcanic regions based on their frequency domain signature, and they presented a different seismic source induced by fast fluid flow into preexisting microcrack networks. Another example is the study of Turkaya et al. (2015) in which they recorded the out-of-plane vibrations of the plates of a Hele-Shaw cell, to be

able to understand the relationship between the solid-fluid-coupled mechanics and the generated acoustic emissions. On a larger scale, a concept of earthquake source mechanics was developed by Stanek and Eisner (2013) to explain the modes which are observed in microseismicity. Their earthquake source concept consists of two incompressible layers with one compressible layer in between, which is subject to fluid pressure. This setup works like a piston pushing the compressible layer leading to large-scale microseismic events. This concept is similar to the experimental setup having two glass plates and a soft porous medium in between, and thus, the mentioned large-scale microseismic events are similar to the acoustic emissions recorded in the experimental setup developed by Turkaya et al. (2015). The out-of-plane plate vibrations in this experimental setup are generated during changes in total stress in the Hele-Shaw cell. The air overpressure in the cell pushes the grains and changes the solid distribution inside the cell. Moreover, the air overpressure varies along the plate. It is higher toward the inlet and decreases toward the semipermeable boundary at the outlet side. By investigating the experimental setup and using the numerical simulations of air-/granular-coupled flow, it can be concluded that the evolution of the total stress map, which is a source of microseismicity, is due to three major effects as described in Turkaya et al. (2015), Niebling et al. (2012a), and Niebling et al. (2012b): (1) air vibrations inside the empty area, (2) pore pressure diffusion into the pores, and (3) solid stress due to compaction. We will here describe the basis of a numerical model taking these effects into account. First, we will explain the physics and mechanics of the simplest flow regimes, which we observe inside the Hele-Shaw cell and then combine these mentioned effects to obtain a more general poroelastoplastic formulation for all the flow conditions we used. Next, we will study the power spectra of out-of-plane plate vibrations created by the process using a code—provided separately in supporting information Data Set S1—that models the pressure, solid stress field, and the resulting wave propagation. We will show how a two power law regime evolves as the channel network evolves, and we will discuss the contributions of the different stress sources on the peaks of the power spectrum and their characteristic properties (frequency band, corner frequency, and power exponents).

2. Constraints for the Numerical Model

2.1. Constraints From the Experimental Study

Here we explain the experimental setup similar to the work previously done by Turkaya et al. (2015), F. K. Eriksen et al. (2017), and F. K. Eriksen et al. (2018). The results from one of the experiments are given in supporting information Text S1 and Movie S2. We are creating a seminumerical model where the evolving boundary conditions are extracted from the experiments for the numerical model. The photos taken during the experiment (980×375 pixels covering the 80×40-cm Hele-Shaw cell surface) are used to determine the geometry of the complex solid-fluid interface. The experiment consists of a Hele-Shaw cell with dimensions 80×40 cm. The cell is made of 1-cm-thick glass plates having 1.5-mm aperture between them. Three boundaries are sealed with a double sided tape, and one boundary on the opposite side of the air inlet is covered with a semipermeable mesh filter (see Figure 1b). This filter lets the fluid leave the system while keeping the grains inside. We inject 2-bar pressure starting from $t = 0$ s similar to a step function. The injection pressure comes from the pressurized tank does not fluctuate during the experiment except the small fluctuations occur around the electrovalve (see supporting information Figure S1). We fill the cell with 80 μm (±1%) Ugelstad spheres (Ugelstad et al., 1992), nonexpanded polystyrene grains. We filled the cell such that a grain-free zone ($\backsimeq$ 5 cm) between the air inlet and the solid-fluid interface is present at the start of the experiment.

In experiments we observed (as in Figures 1a and 1c) that after the start of the injection of air with constant overpressure two zones develop: (1) a zone where the channels empty of grains are formed in the region initially full of grains, while the grains are compacted around these channels, and (2) a zone where the grains are still in loose state. In the compacted zone, we see the grain-free channels. These areas were previously filled with grains but emptied after the start of the injection. Therefore, the stress variations that needs to be modeled are (i) air pressure variations in the grain-free zone, (ii) air pressure variations while the pore pressure diffuses inside the porous medium, and (iii) solid stress variations due to compaction of the granular medium. Using the modeled stress variations, we are also going to model the mechanical vibrations on the glass plates generated by these stress variations so that we can obtain numerically simulated accelerometric recordings to be compared with the ones obtained during the experiments.

The solid fraction $(1 - \phi)$ can be computed as $(1 - \phi) = M_g/(\rho_g V_f) = 0.48$, where ϕ is the porosity inside the cell, $M_g \backsimeq 170$ g is the mass of grains, $\rho_g = 1.05$ g/cm^3 is the density of the granular material, and $V_f \backsimeq 350$ cm^3 is the filled volume of the Hele-Shaw cell in the initial loose state that we would like to model (as measured in

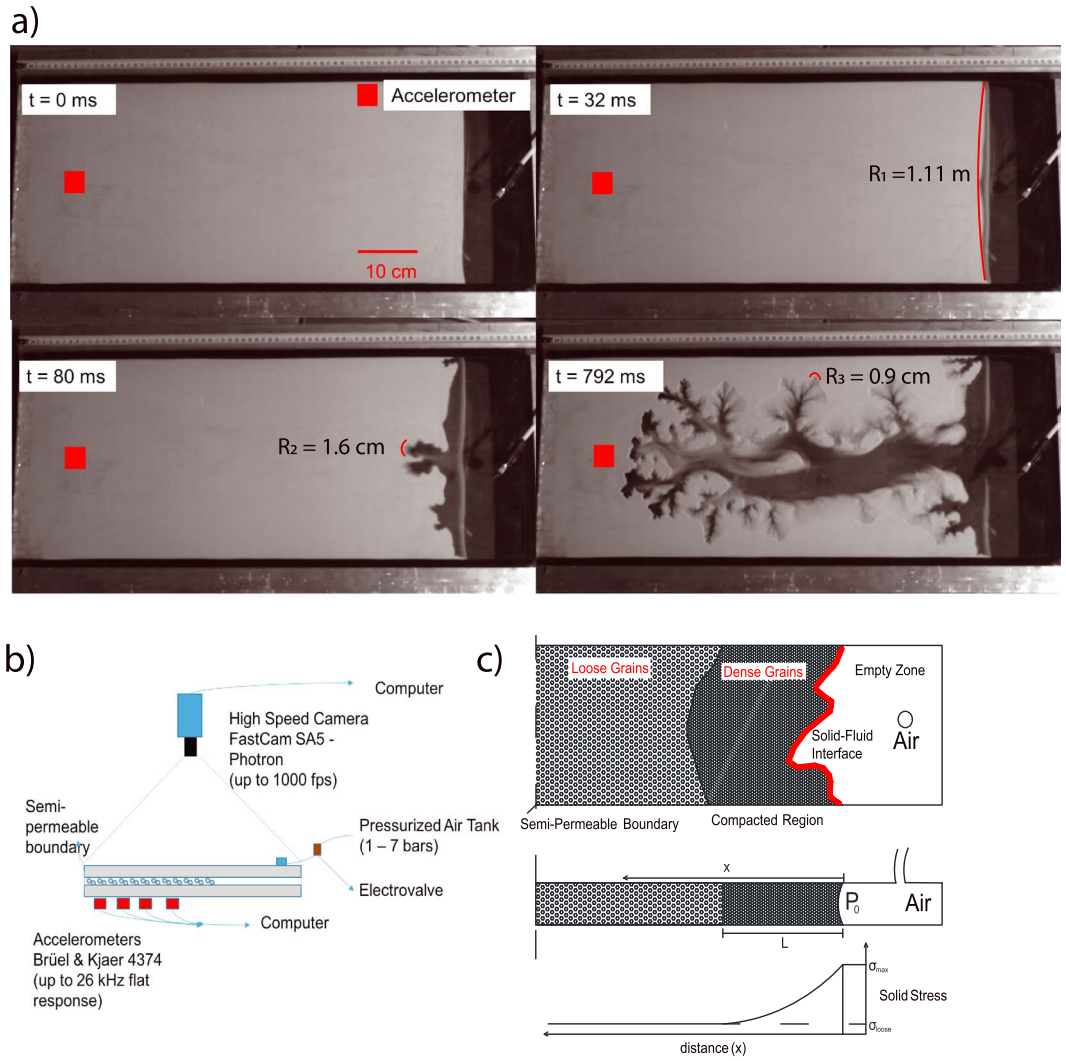

Figure 1. (a) Experimental images showing different stages of the experiment with different radius of curvature (R). (b) Sketch showing the experimental setup. (c) Compaction zone in the Hele-Shaw cell. As the air pushes grains, a compacted zone with a length L occurs. Starting from the fluid-solid interface shown in red, the density of grains (and the solid stress) decreases exponentially along the length x (down to the undeformed phase). The sketch is not in scale.

similar types of experiments by F. K. Eriksen et al., 2017; F. K. Eriksen et al., 2018; Johnsen et al., 2006; Turkaya et al., 2015). Finite size effects due to a quasi 2-D system cause greater porosity values than porosity of random loose packing $\phi_l = 0.41$ (Scott, 1961). In the compaction zone as the solid fraction approaches to random close packing (Berryman, 1983; Scott, 1961), porosity approaches $\phi_c \backsimeq 0.38$.

Figure 1a shows different stages of the experiment. $t = 0$ ms corresponds to the initial state of the Hele-Shaw cell, when the air injection starts. Then ($t = 32$ ms), just after the start of the injection, we observe a quasi-stable compaction phase with a slight curvature of the solid-fluid interface having a very large radius R_1. As we continue injection, the air pushes the grains further eventually breaking the translational symmetry in the direction tangential to the initial front, *fracturing* the porous medium, that is, creating incisions inside the porous medium that present a much smaller radius of curvature R_2. Later on, these incisions split in branches, and further orders of branches develop. Finally, at $t = 792$ ms we have the whole branched structure developed in the system, and this structure remains quasi-stationary for the rest of the experiment. The small fingers present a tip curvature around $R_3 = R = 0.9$ cm, which will be used to calculate the compaction zone in the next section. We are using only one characteristic value of tip radius of curvature (i.e., $R_3 = R$) to simplify the calculations. The permeability values are computed using the Carman-Kozeny equation for porous medium $\kappa_{pore} = \frac{d^2}{180}\frac{(\phi)^3}{(1-\phi)^2}$, where d is the diameter of the grains (Carman, 1937; Turkaya et al., 2015) and for

the channels empty of grains assuming a Poiseuille flow between two plates $\kappa_{empty} = \frac{b^2}{12}$ where b is the channel thickness (i.e., plate aperture in this study; Niebling et al., 2010a; Poiseuille, 1847). For the simulations we used the permeability values:

$$\kappa_{\text{pore}} = 6 \times 10^{-12}\ \text{m}^2$$
$$\kappa_{\text{empty}} = 8 \times 10^{-8}\ \text{m}^2$$

It has been mentioned that the characteristics observed in the Fourier domain are insensitive on the sensor location over the plate in Turkaya et al. (2015) and thus, in the numerical model we are using one accelerometric sensor (Brüel & Kjaer 4374) with an optimal sensitivity in the (1 Hz to 26 kHz) frequency range placed 10 cm away from the semipermeable outlet at the center line of the cell.

2.2. Equations for Air Pressure Calculations Inside the Cell

Air vibration in an empty cavity can be explained and modeled using the classical wave equation for sound waves (Feynman et al., 2011; Royer et al., 1999):

$$\nabla^2 P = \frac{1}{V_s^2}\frac{\partial^2 P}{\partial t^2} \tag{1}$$

where P is the air pressure and V_s is the sound wave velocity in the air. The same equation is valid for chambers with irregular shapes, such as in fingers empty of grains. However, this approach would neglect the air diffusion inside the pores. If we assume that the solid-fluid interface is impermeable, we can get an approximate description of the gas pressure field resonating inside the air channel using equation (1).

However, the solid-fluid interface is permeable. When the overpressure reaches the solid-fluid interface, fluid penetrates into the porous medium and the stress state changes both in the fluid and the solid. Taking into account that the solid part is permeable and assuming that its permeability does not vary significantly over time and that the deformation of the solid part is slow enough compared to the air pressure diffusion, we can use the classical diffusion equation to model this diffusion. The classical pore pressure diffusion equation is given by Biot (1956a) and Biot (1956b) and also used for the same type of experiments by Johnsen, Toussaint, et al. (2008) and Turkaya et al. (2015) as

$$\nabla^2 P = \frac{1}{D}\frac{\partial P}{\partial t}, \tag{2}$$

where $D = \frac{\kappa}{c\phi\mu}$ is the pore pressure diffusion constant, c is the compressibility of the fluid, κ is the permeability of the medium, ϕ is the porosity, and μ is the dynamic viscosity of the fluid. A more refined model taking into account both the vibration of air pressure in empty channels and the pore pressure diffusion regimes in a single framework, amounting to a model of poroplastomechanics, will be developed in the section 3. We will show that in the two limits of high and low porosities, it is equivalent to the two behaviors described here by equations (1) and (2) (i.e., the vibration one and the diffusion one respectively).

2.3. Equations Describing the Out-of-Plane Stress Calculations

During fracturing, the state of stress in the solid part changes as well. To create thin fingers, there is a stress threshold to be passed. For a mode 1 fracturation this is due to humidity and capillary bridges between the grains and for a mode 2 fracturation this is due to the friction between the grains and the friction between the grains sliding against the glass plates. In the considered case, the Hele-Shaw cell has a semipermeable boundary at the outlet, which prevents the grains to leave the cell. Hence, compaction in the porous medium is the only way to create grain-free channels, that is, areas empty of grains inside the medium which is only possible if the surrounding grains slide on the glass plates. In the granular medium, starting from the clean fluid-granular medium boundary (i.e., the red interface shown in Figure 1c), there is a region where the grains are compacted into a densely packed configuration. This region is called the compaction front. Starting from the compaction front, at distance x from the boundary between empty fingers and compacted grains, we can obtain the out-of-plane solid stress $\sigma_{zz}(x)$, as presented in earlier works of Knudsen et al. (2008), Sandnes et al. (2011), and J. A. Eriksen et al. (2018) as

$$\sigma_{zz}(x) = \frac{\rho_s g \Delta z}{2}\left[\{\psi\gamma + 1\}\, e^{\frac{2\gamma\psi(L-x)}{\Delta z}} - 1\right], \tag{3}$$

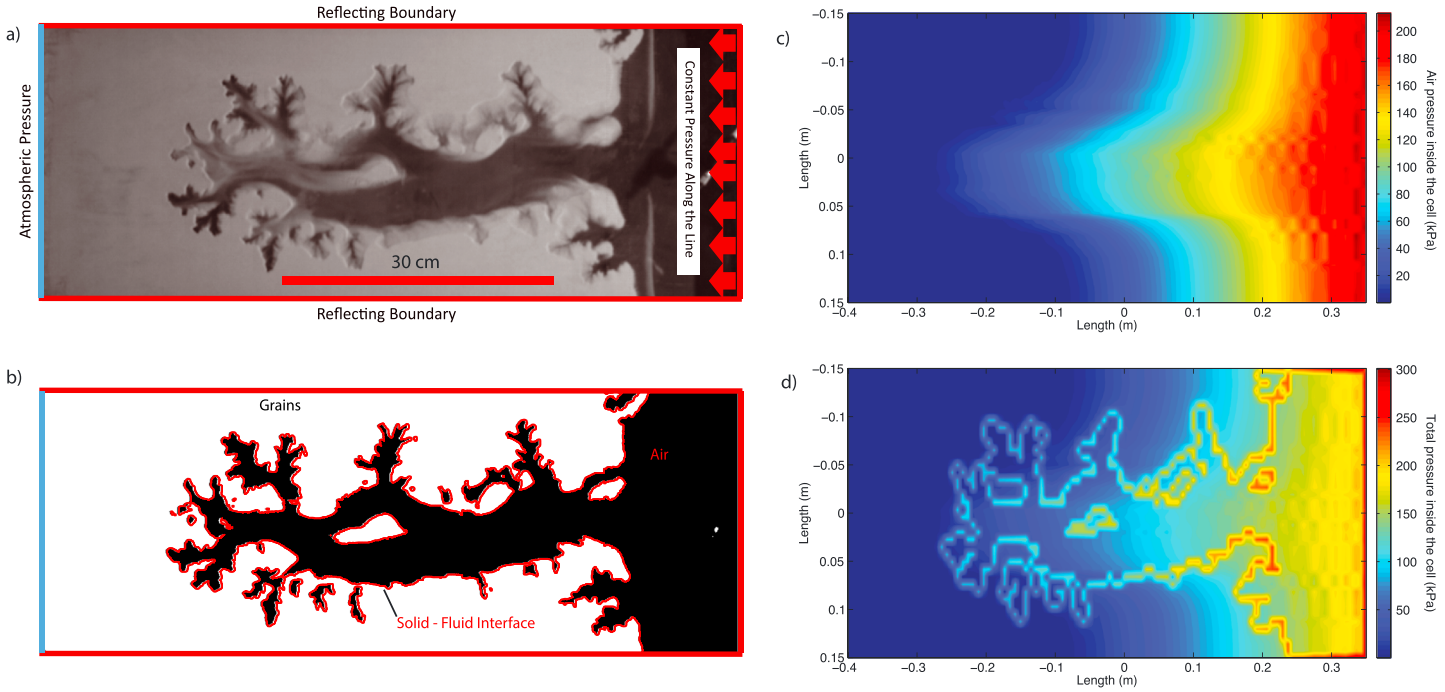

Figure 2. An image of the Hele-Shaw Cell during injection $t = 0.536$ s is presented with the numerical simulation results. (a) Photo of the Hele-Shaw cell with boundary conditions identified. (b) Binarized image of the porous medium allow us to numerically separate the solid matrix (white) from the grain-free zone (black). The solid-fluid interface is drawn with a red line along the grain-free zone. (c) The simulated air pressure using equation (19) is presented for this snapshot. (d) The simulated total stress found using equation (20) is presented for this snapshot. Color bars show the pressure in normal direction to the glass plate in kilopascals.

where $L = \frac{\phi_n R}{(1-\phi_n)}$ is the thickness of the compaction front (see Figure 1c) with typically $L = 3$ cm, where ϕ_n is the normalized solid fraction $\phi_n = (1-\phi)/(1-\phi_c)$. $\Delta z = 1.5$ mm is the aperture of the Hele-Shaw cell, and ψ is the Janssen's coefficient as given in Janssen (1895), Knudsen et al. (2008), and Sandnes et al. (2011). We considered $\psi = 1$ in this study, which is a typical value in order of magnitude as discussed in these references. γ is the friction coefficient between the grains and plates considered as 0.3, $\rho_s = (1-\phi)\rho_g = 0.5$ g/cm^3 is the initial effective density of the granular medium and x is the distance from the solid-fluid interface (see Figure 1c). This stress profile can be solved with equation (3) to determine the map of the out-of-plane solid stress inside the cell at a specific time t.

Inside the cell, variations of normal stress and tangential stress generate vibrations in a direction normal to the plate surface. Note that the amplitude ratio of the out-of-plane vibrations induced by normal stress in comparison to the vibrations induced by tangential stress is typically of about 5–10 times larger due to the elastic properties of a thin 2-D plate (Royer et al., 1999). This was experimentally verified by recording the vibrations on different axes of the plate generated by an impact force normal to the plate (see supporting information Text S2 and Figure S2 for details; Janssen, 1895; Kausel, 2013). Therefore, in what follows we neglect the tangential stress component on the simulation of vibrations in a direction normal to the plate surface.

In Figures 2c and 2d we present the snapshots of air and total stress maps in normal direction on the top glass plate of the Hele-Shaw cell. These pressure maps vary with time, and these variations of pressure generate vibrations on the plates of the Hele-Shaw cell. Specifically in 2-D thin plates, these vibrations are called Lamb Waves (Lamb, 1904; Royer et al., 1999). By convolving the stress variations on each pixel to the far-field Lamb wave approximation presented in Goyder and White (1980), as detailed further in section 2.4, we obtain the out-of-plane vibrations on the plate, which correspond to the vibrations recorded by the accelerometers during the experiments.

In this study, as presented in the experimental work, we expect the power spectrum of the out-of-plane plate acceleration to evolve as the channel network develops. The experimental and numerical results will be compared in various aspects in section 4.2.

2.4. Accelerometric Signal Generation Across the Plate

We want to compare the experimentally recorded and simulated vibrations at one side of the plate. Therefore, we need to generate numerical out-of-plane mechanical vibrations occurring due to stress fluctuations inside the Hele-Shaw cell. The vibrational displacements on a plate $u(x_r, y_r, t)$ observed on a position (x_r, y_r) and over time t due to a force F exerted on the point (x_s, y_s) can be expressed as given in Aki and Richards (2002) and Farin et al. (2016):

$$u(x_s, y_s, t) = \int\int\int \tilde{G}(x_r, y_r, \omega_r; x_s, y_s, \omega_s) * \tilde{F}(x_s, y_s, \omega_s) \mathrm{d}x\mathrm{d}y\mathrm{d}\omega \tag{4}$$

where $*$ is the convolution product and $\tilde{G}(x_s, y_s, t)$ is the Green function of the waveguide. Here $\tilde{F}$ is the Fourier transform of the force exerted on a point computed by multiplying the total stress simulated on a pixel with the pixel area. In this study the resolution is set to $\approx 60\,\mathrm{mm}^2$ per pixel. In other experiments where the mechanical vibrations are generated in plates by a stress exerted on plates, equation (4) is expressed as a far-field approximation of the Lamb waves (Farin et al., 2016; Goyder & White, 1980; Turkaya et al., 2016) :

$$\tilde{\xi}(l, \omega(k)) = \frac{-i\tilde{F}(\omega(k))}{8Bk^2}\sqrt{\frac{2}{lk\pi}}e^{-i(lk-\pi/4)} \tag{5}$$

where $\tilde{\xi}(l, \omega(k))$ is the displacement of the plate in Fourier domain at a distance $l = \sqrt{(x_s - x_r)^2 + (y_s - y_r)^2}$ from the source, $\tilde{F}(\omega(k))$ is the applied force in Fourier domain at a point like source, B is the bending stiffness $B = \frac{h^3 E}{12(1-\nu^2)}$ where h is the thickness of the plate, E is the Young's modulus, and ν is the Poisson's ratio of the plate material. k is the wavenumber where the dispersion relation with angular frequency ω is $k = \omega^{1/2}\left(\frac{\rho h}{B}\right)^{1/4}$. If the frequency is higher than the cutoff frequency of the dispersion relation (which satisfies $kh \simeq 1$), then the dispersion relation will become $\frac{\omega}{k} = \frac{\mathrm{d}\omega}{\mathrm{d}k} \approx V_R$ where V_R is the Rayleigh Wave velocity on the plate surface (Royer et al., 1999). To compare simulation data with accelerometric recordings, we need to obtain the power spectrum of the accelerations on the plate surface, which is the double derivative of the displacement; thus, equation (5) becomes (Farin et al., 2016; Royer et al., 1999)

$$\tilde{\alpha}(l, \omega(k)) = [\tilde{\xi}(l, \omega(k))\omega(k)^2]^2 \tag{6}$$

where $\tilde{\alpha}$ is the power spectral amplitude. To keep the vibrations simple, in the numerical studies, we did not include the reflections on the side boundaries. Even though this may cause some differences in the amplitude on the power spectral distribution curves, the main structure which is the essential part of this study remains the same, as we checked in comparisons with simulations where we included them.

3. Numerical Modeling of Air Pressure

We start with the Navier-Stokes equation (Guyon et al., 2001), describing a fluid mixed with solids at an elementary representative scale of ~ 10 grains size (i.e., scale corresponding to the Darcy equation; Darcy, 1856), with a momentum exchange term between the solid and fluid linear in relative velocity as in Niebling et al. (2010a), Jackson (2000), and Van der Hoef et al. (2006):

$$\rho_f \frac{\partial}{\partial t}(\mathbf{v_f}) = -\nabla P - \frac{\mathbf{v_f} - \mathbf{u}}{\kappa}\mu\phi, \tag{7}$$

where ρ_f is the density of the injected air, ϕ is the porosity, $\mathbf{v_f}$ is the average velocity of the air, $\mathbf{u}$ is the granular velocity, μ is the viscosity of the air, and κ is the permeability of the medium. From equation (7) we express $\mathbf{v_f}$ as

$$\mathbf{v_f} = \mathbf{u} - \frac{\kappa}{\phi\mu}\left(\nabla P + \rho_f \frac{\partial(\mathbf{v_f})}{\partial t}\right). \tag{8}$$

During this coupled flow, the mass (both of air and grains) is preserved. Thus, the stresses inside the Hele-Shaw cell can be explained with the mass conservation equations of the air and solid phases similarly used in Johnsen, Toussaint, et al. (2008), Niebling et al. (2010a), and Niebling et al. (2010b). For the air phase, mass conservation can be written as

$$\frac{\partial}{\partial t}(\rho_f \phi) + \nabla \cdot (\rho_f \phi \mathbf{v_f}) = 0, \tag{9}$$

Implementing $\mathbf{v_f}$ from equation (8) in equation (9), we have

$$\frac{\partial}{\partial t}(\rho_f \phi) + \nabla \cdot \left(\rho_f \phi \left[\mathbf{u} - \frac{\kappa}{\phi \mu} \nabla P \right] - \frac{\rho_f^2 \kappa}{\mu} \frac{\partial \mathbf{v_f}}{\partial t} \right) = 0, \tag{10}$$

Taking into account that the air is compressible, the change in the air mass density can be expressed linearly as

$$\rho_f = \rho_0 + \rho_0 c (P - P_0) \tag{11}$$

where ρ_0 is the reference density of air at atmospheric pressure and room temperature and $c = 1/P_0$ is the isentropic compressibility of the air—considering air as an ideal gas. For the grains the mass conservation equation is

$$\frac{\partial}{\partial t}(1 - \phi) + \nabla \cdot ((1 - \phi)\mathbf{u}) = 0. \tag{12}$$

which can be simplified into $\frac{\partial \phi}{\partial t} = -\mathbf{u} \cdot \nabla \phi + (1 - \phi) \nabla \cdot \mathbf{u}$. Inside the pores, taking into account the equation of state of the air (equation (11), equation(10) will transform to

$$\phi \rho_0 \frac{\partial P}{\partial t} + \rho_f \frac{\partial \phi}{\partial t} = \nabla \cdot \left[\rho_f \frac{\kappa}{\mu} \nabla P \right] - \nabla \cdot (\phi \rho_f \mathbf{u}) + \nabla \cdot \left(\frac{\rho_f^2 \kappa}{\mu} \frac{\partial \mathbf{v_f}}{\partial t} \right). \tag{13}$$

Two terms of equation (13) can also be expressed using equation (12); we can get

$$\rho_f \frac{\partial \phi}{\partial t} + \nabla \cdot (\phi \rho_f \mathbf{u}) = \rho_f \nabla \cdot [(1 - \phi)\mathbf{u}] + \nabla \cdot [\phi \rho_f \mathbf{u}], \tag{14}$$

which simplifies to

$$\rho_f \frac{\partial \phi}{\partial t} + \nabla \cdot (\phi \rho_f \mathbf{u}) = \rho_f \nabla \cdot \mathbf{u} + \mathbf{u} \phi \nabla \rho_f \tag{15}$$

expanding the left term of equation (15) with equation (11) we get

$$\rho_f \frac{\partial \phi}{\partial t} + \nabla \cdot (\phi \rho_f \mathbf{u}) = \rho_f \nabla \cdot \mathbf{u} + \phi \rho_0 c \mathbf{u} \cdot \nabla P. \tag{16}$$

Putting equation (16) into equation (13), we get

$$\begin{aligned} \phi \rho_0 c \left[\frac{\partial P}{\partial t} + \mathbf{u} \cdot \nabla P \right] &= \nabla \cdot \left[\rho_f \frac{\kappa}{\mu} \nabla P \right] \\ &+ \nabla \cdot \left[\frac{\rho_f^2 \kappa}{\mu} \frac{\partial \mathbf{v_f}}{\partial t} \right] \\ &- \rho_f \nabla \cdot \mathbf{u} \end{aligned} \tag{17}$$

which is equal to

$$\begin{aligned} \phi \left[\frac{\partial P}{\partial t} + \mathbf{u} \cdot \nabla P \right] = \nabla \cdot \left[\hat{P} \frac{\kappa}{\mu} \nabla P \right] - \hat{P} \nabla \cdot \mathbf{u} \\ + \nabla \cdot \left[\frac{\rho_f^2 \kappa}{\rho_0 c \mu} \frac{\partial \mathbf{v_f}}{\partial t} \right] \end{aligned} \tag{18}$$

where $\hat{P} = \frac{\rho_f}{\rho_0 c} = P - P_0 + 1/c$, which comes from equation (11). It should be noted that inside the pores, the air pressure fluctuations are small compared to the background pressure, which leads to $\hat{P} \approx P_0$ (Niebling et al., 2010b). We can apply some simplifications to equation (18): (i) In a fluid without porous medium, $\nabla \cdot \left[\frac{\rho_f \kappa}{\rho_0 c \mu} \frac{\partial \mathbf{v_f}}{\partial t} \right]$ reduces to $\frac{\rho_f \kappa}{\rho_0 c \mu} \frac{\partial \nabla \cdot \mathbf{v_f}}{\partial t}$. (ii) Considering that the local variations in density of the fluid and porosity are negligible compared to the fluid velocity variations, we can simplify equation (9) to obtain $\nabla \cdot (\rho_f \phi \mathbf{v_f}) \sim \rho_f \phi \nabla \cdot (\mathbf{v_f})$. This assumption is numerically validated, and the resulting values can be seen in supporting information Figure S3. (iii) Third, we can write $-\frac{\partial}{\partial t}(\rho_f \phi) \sim -\phi \frac{\partial}{\partial t}(\rho_f) \sim -\phi c \rho_0 \frac{\partial}{\partial t}(P)$ taking into account that the porosity is hardly varying over time in the granular medium, and approximated as constant, variations over time in the density of the fluid are expressed using the compressibility equation (equation (11). (iv) Using (ii) and (iii), we write $c \frac{\partial P}{\partial t} \sim \nabla \cdot \mathbf{v_f}$ then evolving this to use in equation (18) we get $-c \frac{\partial^2 P}{\partial t^2} \sim \frac{\partial \nabla \cdot \mathbf{v_f}}{\partial t}$.

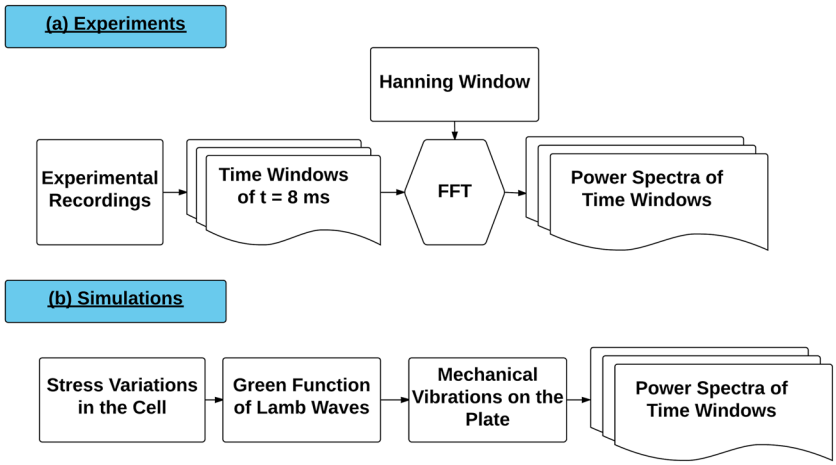

Figure 3. The sequence of the experimental and simulation data analysis. (a) The experimentally recorded signal is split into 8-ms time windows, then treated using a Hanning Window (Oppenheim, 1999) to remove the effect of discretization. Afterward, a fast Fourier transform (FFT) is applied and the resulting spectra are squared to obtain the experimental power spectra. (b) Using equation (20) stress variations inside the cell are computed, afterward the computed stress variations are convolved with the Green's function for Lamb waves (Goyder & White, 1980) to calculate the displacements on the glass plates. Next, these displacements are converted to power spectra of the plate acceleration as given in equation (6). Eventually, the evolution of these vibrations are compared with the evolving state of solid-fluid interactions inside the Hele-Shaw cell.

Applying all these simplifications, we eventually obtain the formulation that accounts for the air vibrations in the empty area and the pressure diffusion in the porous medium:

$$\left[\frac{\partial P}{\partial t} + \mathbf{u}\cdot\nabla P\right] = \nabla\cdot\left[\hat{P}\frac{\kappa}{\mu\phi}\nabla P\right] - \hat{P}\nabla\cdot\mathbf{u} - \frac{\rho_f^2\kappa}{\rho_0\mu\phi}\frac{\partial^2 P}{\partial t^2}. \tag{19}$$

When κ is large (i.e., in the empty channels where $\hat{P}$, κ, μ, and ϕ are constant), the first and third term of the right-hand-side dominate and assuming that ρ_f is close to ρ_0, equation (19) reduces to $\hat{P}\nabla^2 P - \rho_f\frac{\partial^2 P}{\partial t^2} = 0$. Knowing that $\frac{\hat{P}}{\rho_f} = c = {V_s}^2$, where V_s is the sound wave velocity, we can obtain the air vibration equation in the empty channels equation (1) that we defined in the introduction. Moreover, if κ is small (i.e., in the pores when there is no active deformation), the last term vanishes and the equation (19) boils down to equation (2). We note that the equation (19) behaves asymptotically as the equations corresponding to vibration of perfect fluid in channels and fluid pressure in pores.

To compute the granular velocity **u**, we subtracted the experimental images that are taken with 8-ms time steps. The velocity of the grains are calculated inside the porous medium in the compaction zone along the interface and decayed linearly to zero over a length proportional to the extent L of the compaction zone as seen in Figure 1c.

Furthermore, by adding the fluid stress equation (19) to the solid stress computed via equation (3) one can compute the total stress exerting on the glass plates in normal direction as

$$\sigma_{\text{Total}} = P + \sigma_{zz} \tag{20}$$

Solving equation (19), equation (3), and then eventually equation (20) with a forward finite difference scheme as explained in supporting information Text S3 (Levy & Lessman, 1961), we obtain the full field stress maps as seen in Figure 2. As shown in Figure 2a, the pressure is applied at the right boundary from time zero as a line source and kept constant through time. The boundaries at the top and bottom are sealed, and the boundary on the left is fixed to atmospheric pressure (i.e., overpressure $P = 0$). Using the binarized experimental image in Figure 2b, the solid-fluid interface is extracted for pressure computation. Figure 2c shows the air pressure field inside the Hele-Shaw cell. In the total pressure map as presented in Figure 2d, we see that the compaction zone in the solid is subject to higher pressures. The corresponding color bar shows the pressure applied on the plate in kilopascals.

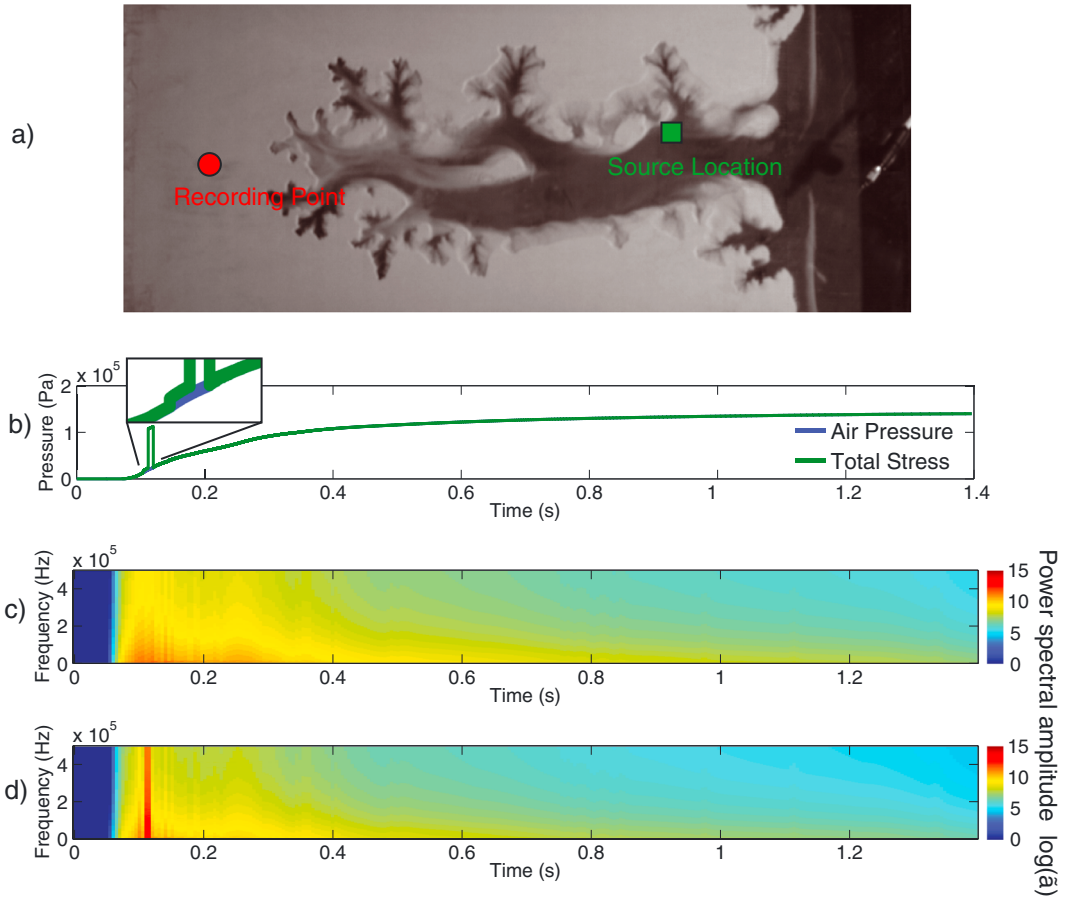

Figure 4. Power spectral evolution of the Lamb waves on the plate compared with the different types of loading. (a) A photo of the Hele-Shaw cell at $t = 0.536$ s with the locations of recording and source points indicated. A green square where the source is sampled, and a red circle where the mechanical vibrations (Lamb waves) due to stress variations are numerically modeled. (b) Air pressure and total stress sampled (numerically) on the green square over time. (c) Power spectrum of the Lamb waves due to air pressure simulated on the recording point. (d) Power spectrum of the Lamb waves due to total stress simulated on the recording point.

As described in Figure 3a, 8 ms of time windows are obtained using the raw experimental recordings. Each time window is treated using a Hanning Window right before transformation into Fourier domain to avoid any artifacts of discretization (Oppenheim, 1999). Then the spectra in Fourier domain are squared to obtain the power spectrum corresponding to each time window as explained in Turkaya et al. (2015). In the simulations, this procedure is slightly different (see Figure 3b). First, the stress map on the plate for a snapshot in time is computed using equation (20). Then, we calculate the mechanical vibrations on the plate occurring due to the variations of stress in subsequent snapshots. Using the full field stress variations inside the Hele-Shaw cell, the mechanical vibrations on the glass plates are generated by convolution of a point force variation with the Green's function for Lamb waves (Goyder & White, 1980) using equation (5). This convolution is explained in detail in section 2.4. Following this, these power spectra are compared to study the evolution of characteristic features of these vibrations in relation with the solid-fluid interactions inside the Hele-Shaw Cell.

4. Results and Discussion

4.1. Numerical Simulation Results

The mechanical vibrations of the plates at the recording point are generated by the variations of the stresses (solid and/or fluid) exerted on the glass plates of the Hele-Shaw cell. First, we look at the vibration contribution of one grid point source. Furthermore, we can decompose the applied force to fluid pressure and total stress as in equation (20).

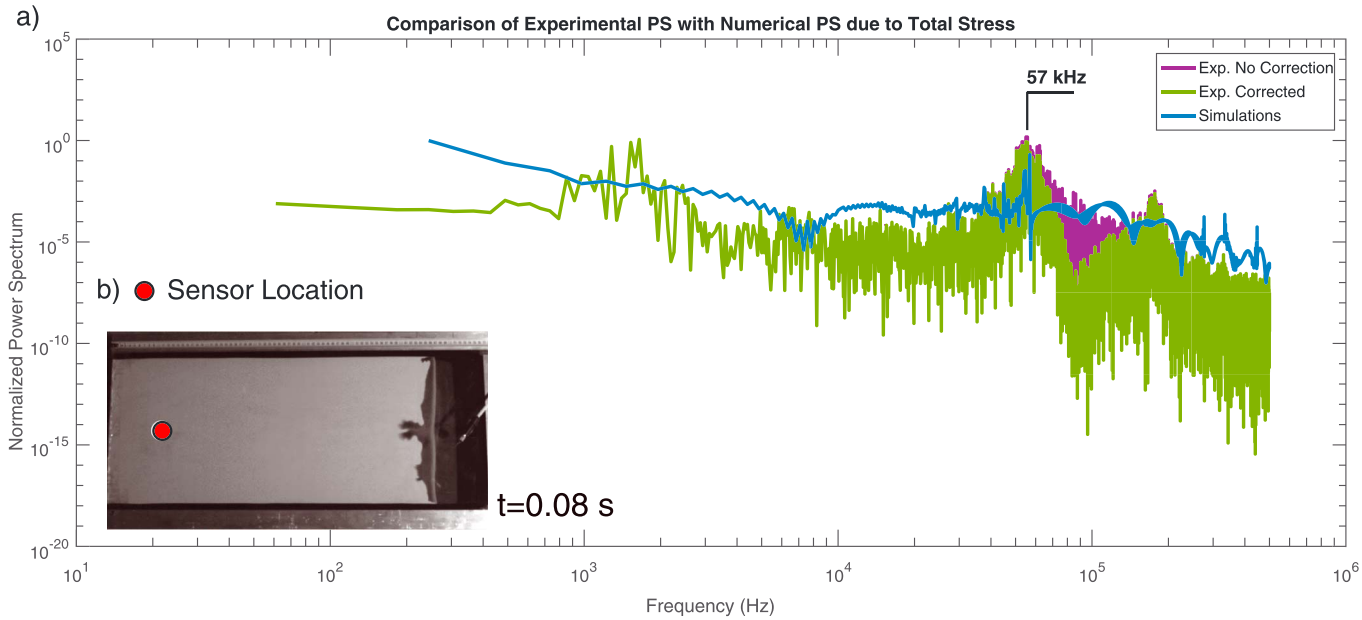

Figure 5. Comparison of a numerical and an experimental (normalized) power spectra corresponding to the t = 0.08 s. (a) Violet curve shows the raw signal. Green curve shows the signal corrected by extending the manufacturer's calibration curve for the high frequencies. Blue curve shows the simulated power spectrum using full field total stress variations. (b) Snapshot of the Hele-Shaw cell to the moment corresponding to power spectra. Marker shows the sensor location.

In Figure 4a we present a simple case that is having one spatial source over the plate (green square) and the vibrations are simulated on a single recording point (red circle) placed 10 cm away from the semipermeable boundary along the line of the inlet. Figure 4b shows the air pressure and total stress evolution over time on the sampling point (green square of Figure 4a). A zoomed window is attached to illustrate that around $t = 0.1$ s there is a jump on the total stress which is not present in the air pressure. Considering equation (20), we can say that this sudden increase is due to the solid stress increase on the grid point corresponding to the source location. Furthermore, we compare the generated power spectra. In Figure 4c, a spectrogram (equation (6) due to the vibrations generated by the air pressure P is shown. This spectrogram is prepared by taking 8-ms discrete time windows of stress variation on the plate and convolving with equation (5) to obtain the power spectrum of each window. Figure 4d shows at the same time the spectrogram of the vibrations generated by the total stress in the cell (see supporting information Movie S1 for the corresponding movie of the stress evolution). It can be seen that, with the initial increase of the injection pressure, the power spectrum becomes more energetic $E \propto \int_{-\infty}^{\infty} |\tilde{\alpha}(l, \omega(k))|\, \mathrm{d}\omega$ where E is the signal energy as defined by Parseval's Theorem (Bracewell, 2000).

The difference in these two curves observed in Figure 4b appears when the compaction zone passes through the point taken as the source. Thus, we say that the source corresponding to fluid pressure variations dominates over solid stress variations, except when the compaction front is close to the sensor. The spike in the loading corresponds to the time when the compaction front passes through the source point. At this moment we observe in Figure 4d that the power spectrum has an abrupt increase at all frequencies. Following this, the source point remains in the empty area, where the air is bursting into the empty channel giving power to the low-frequency range of the spectrum. As the air penetrates into the pores toward the boundary open to atmosphere, the pore pressure fluctuations and the vibrations diminish, leading to a decay in the power spectrum. To study the effect of possible inlet pressure fluctuations, we simply add Gaussian white noise noncorrelated in time on the air injection data and repeat the procedure seen in Figure 4. The signal to noise ratio is set to 30 dB. The application of noise covers the structures present in the power spectrum in all frequencies and makes it difficult to see the structures that we would like to identify. Supporting information Figure S4 comparing the power spectral evolution with and without noise is provided in supplementary material. We can say that the noise in the injection pressure covers the signature evolution in the power spectrum. For a better linking between the mechanics of the solid-fluid mechanics with corresponding microseismic events, it is preferred to not to include fluctuations of the inlet pressure in the numerical simulations.

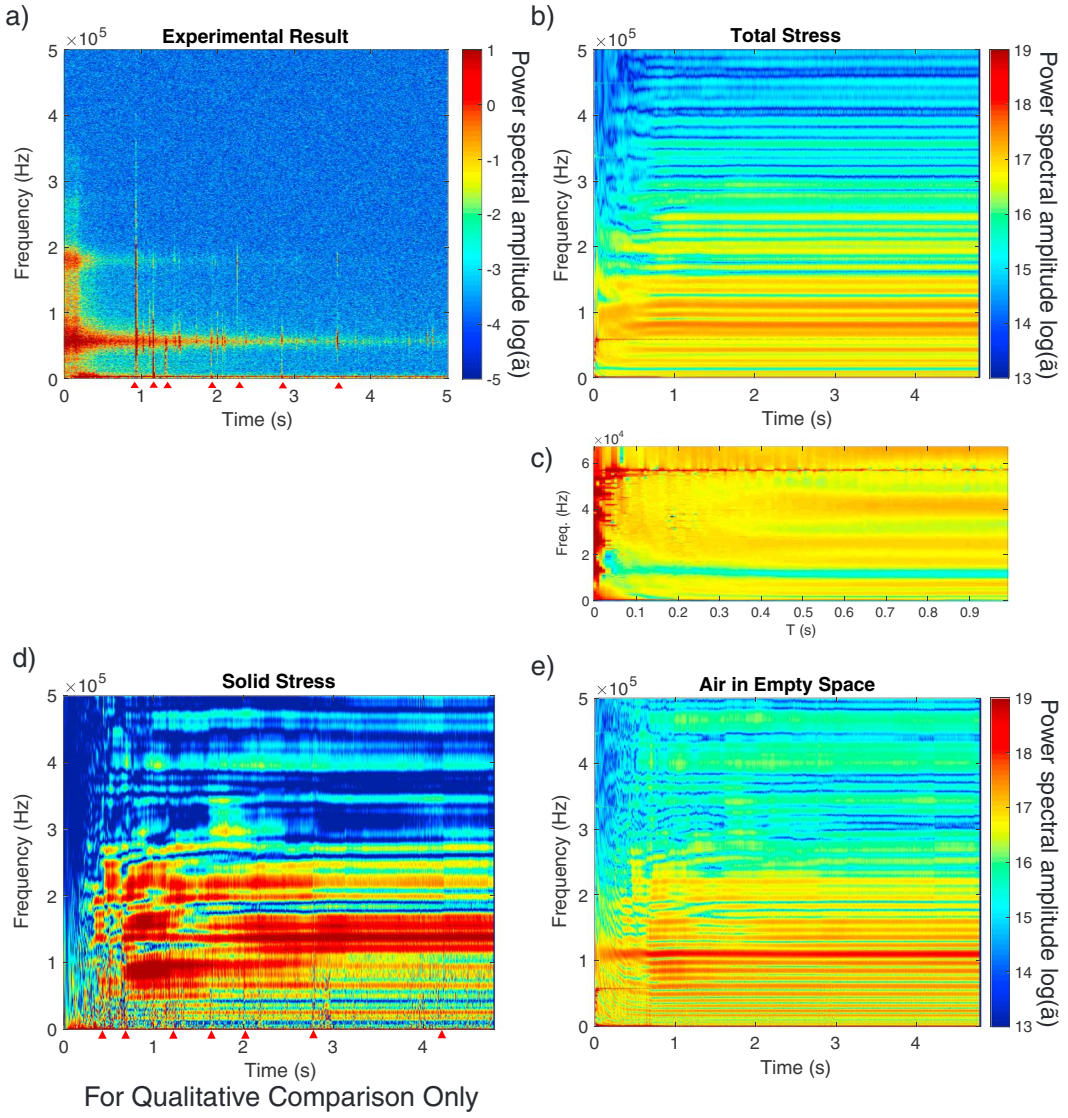

Figure 6. Comparison of power spectra obtained from experimentally recorded data and obtained using different stresses as vibration source in numerical simulations. (a) Experimental power spectra with red arrow markers showing stick-slip events, (b, c) simulated power spectra using total stress and a zoomed version on the peak around 57 kHz. (d) Numerical simulations using solid stress as a source; red arrows mark the abrupt changes as vertical lines. (e) Simulated power spectra using air pressure in empty space. Color bars are given in log scale.

4.2. Comparison of the Experiments and the Numerical Simulations

To compare the numerical simulations with the experimental results, we need to numerically simulate the experimentally recorded vibrations on a sensor location generated by the full field stress variations over the cell. In other words, if we repeat the procedure that we did in Figure 4 for all the grid points on the plate, we obtain the simulated accelerometric recordings. Considering the acceleration generated by the total stress, and focusing on the signal over a window 8-ms duration centered on time $t = 0.08$ s after the start of the experiment, we can compare the power spectrum of the experimental signal and the simulated one directly. In Figure 5, we see that even though the two power spectra does not have a perfect match there are several things in common. First, both spectra have a plateau across the lower frequencies until a peak and then a slope in the high-frequency region starting right after the peak. Furthermore, both of them have a peak around 57 kHz, which shows that the stresses simulated inside the Hele-Shaw cell are able to represent a part of the signature that we see in the experiments. However, there are some differences between these curves as well. Up to 10 kHz the structures are very different. This difference happens because the stress variations are discretized with 8-ms steps, which is not long enough to capture the characteristics of the low-frequency

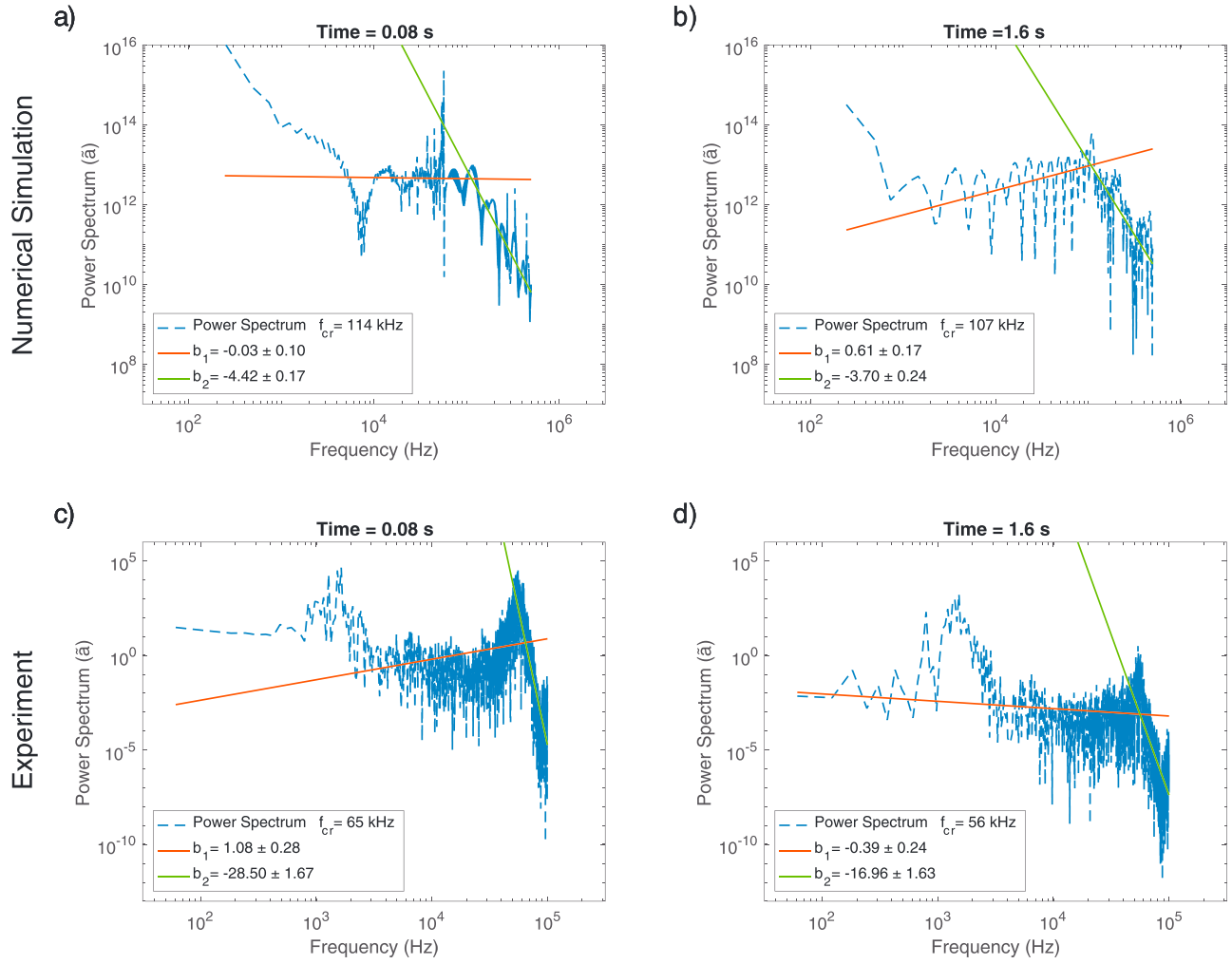

Figure 7. Power law evolution and comparison of numerical (a, b) and experimental (c, d) power spectra. Numerical simulations of total stress normal to the plate and experimentally recorded signals are used to generate the power spectra at times t = 0.8 s and t = 1.6 s. Each subfigure has two power law fits ($ax^b = y$). The point of coincidence of the fitting curves is marked to define the corner frequency.

signals correctly. This duration is limited with 8 ms because a longer-signal duration will cause reflections from the sides to cover the signature that we would like to see in the simulated power spectrum.

Next, we investigate further the power spectrum evolution by observing the spectra belonging to all time windows (8 ms each). In Figure 6 we compare the experimentally recorded spectra (Figure 6a) with spectra simulated using total stress (Figures 6b and 6c), solid stress (Figure 6d), and air pressure in empty channels (Figure 6e) separately. In Figure 6a, we compare the experimental and numerical (total stress) power spectra. One can observe that the largest peak that is dominating the experimental power spectra (at 57 kHz) is present in the numerical simulation results as well (Figure 6c). These peaks are wider at the start of the injection and thinner toward the end of fracturing. In Figure 6e, we search this peak further by calculating only the vibrations due to air pressure in channels empty of grains inside the Hele-Shaw cell. Therefore, we say that the air pressure is the main generating factor of the peak at 57 kHz. Then we compare the power spectra coming from the experimental recordings and from the numerically generated vibrations using only solid stresses as seen in Figure 6d. As expected, we do not see the main peaks noticed in Figures 6a and 6b but the vertical thin lines corresponding to the events generated due to the sudden stress rearrangements inside the porous medium with the effect of pore pressure diffusion defined by Turkaya et al. (2015; called Type 2 events in the article). These events have a stick-slip nature, and they are intermittent. As defined in the same article, the rate of occurrence of these events is diminishing as injection goes on. This is also visible in the numerically obtained results. The time of the markers can be fit with an Modified Omori law as done in Turkaya et al. (2015) giving

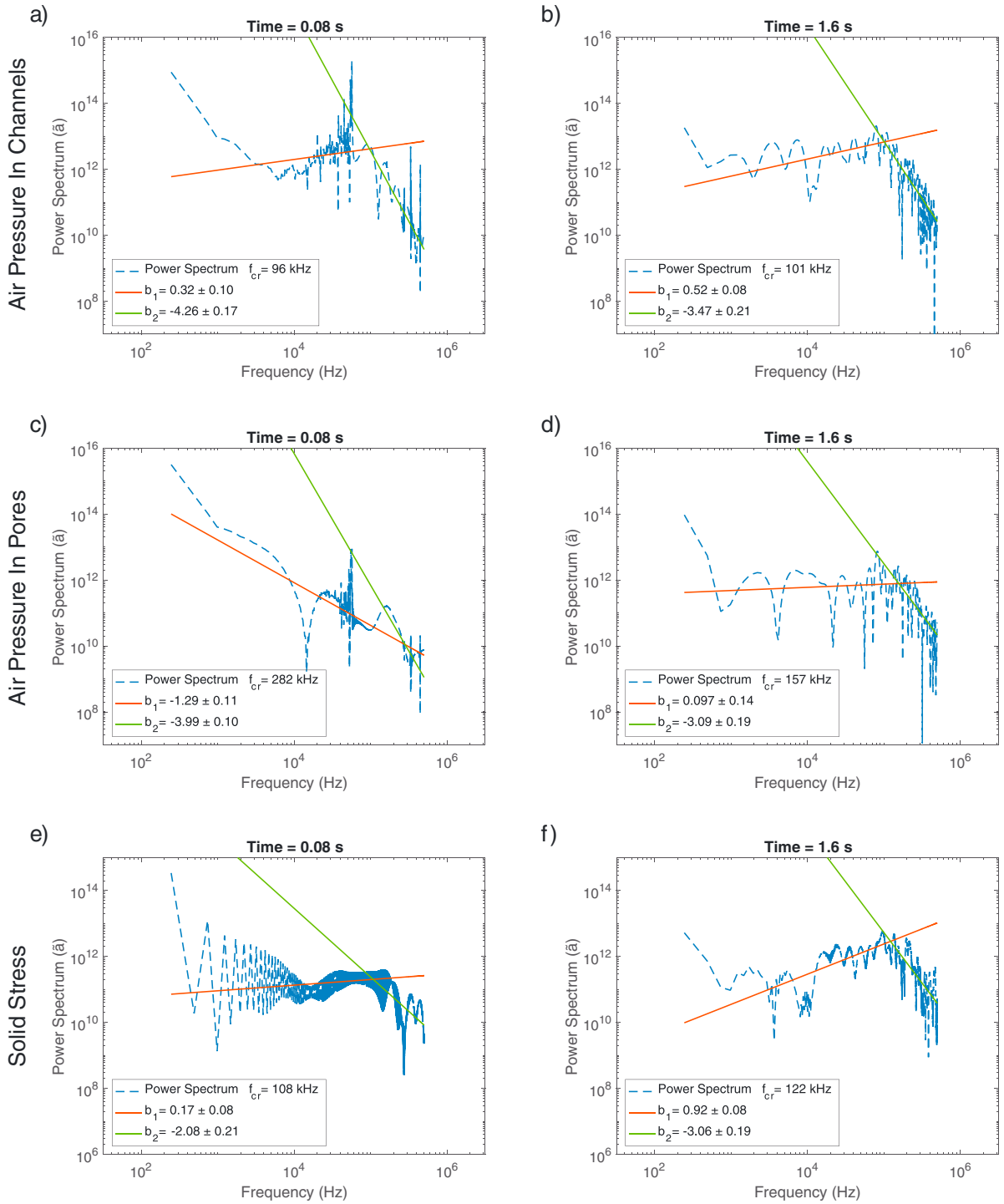

Figure 8. Power law evolution and comparison of power spectra due to different pressure contributions. (a, b) Only the air pressure in empty channels, (c, d) the air pressure inside the porous medium, and (e, f) solid stress normal to the plate are used to generate the power spectra at times $t = 0.8$ s and $t = 1.6$ s. Each subfigure has two power law fits ($ax^b = y$). The point of coincidence of the fitting curves is marked to define the corner frequency.

p = 0.55, which is in the same range calculated for the same type of experiments. The details of this fit is explained in supporting information Text S5.

Furthermore, by using curve fitting and comparing the fitting parameters, we can perform a quantitative comparison between experiments and simulations. In Figure 7, we compare the power spectra of specific time windows at t = 0.8 s and t = 1.6 s obtained using the numerically simulated plate vibrations due to total stress applied normal to the plate (Figures 7a and 7b) and using the experimental recordings (Figures 7c and 7d). The exponents (slope) $b1$ and $b2$ are obtained after filtering the signal with a low-pass and high-pass filter having a 60-kHz cutoff frequency (chosen with respect to the peak frequency), respectively. Next, we calculated the corner frequency as where the two linear fitting lines having slopes $b1$ and $b2$ coincide. We observed, in both cases, that after the first $t \approx 0.1$ s the corner frequency fluctuates $\approx$ 10% but stays in the same order of magnitude. In supporting information Figures S5 and S6 the figure panels are identical to Figure 7 but they show more time steps for different pressure contributions. In addition, supporting information Figures S7–S12 are provided to show the evolution of the mentioned fitting parameters a, b and the corner frequency f_{cr}. We also provide supporting information Figure S13 comparing the experimental and numerically simulated accelerations in the time domain.

4.3. Discussion

By looking at the power spectra in different snapshots of time belonging to different contributions on the recorded vibrations in Figure 8, we can say that the air pressure vibrations are dominating the signal of total stress. These vibrations in Figures 8a–8d (the contribution of air) are particularly in midrange frequency of the power spectrum from 1–2 up to 60 kHz. Low-frequency signals with frequencies up to 20 kHz are mentioned in the experimental study (Turkaya et al., 2015) for a smaller pressure level. Here the maximum peak is recorded to around 57 kHz as seen in Figure 6. The developing channels in this system are fractal in shape, as can be seen in the optical data, and as analyzed in detail in F. K. Eriksen et al. (2017) and F. K. Eriksen et al. (2018). Their box-counting fractal dimension is around 1.5 to 1.7. Note that the channels are natural fractal-like patterns; that is, they are only self-similar over a limited range of scales as opposed to perfect fractals, which are self-similar on all scales. Here we have observed that the channels are self-similar on scales from the smallest channels $\sim 10^{-2}$ m up to the cell size $\sim 10^{0}$ m. These structures grow from an initially simple geometry and once they are established, the power spectrum of the acoustic emissions can be fitted with two different power law curves. The vibration of the air in such cavities, or the solid stress evolving along such boundaries, or the air pressure diffusing from such boundaries, could be responsible for the similarities with power law. Although some features of the channels are fractal, there are also many characteristic scales in the problem (pore size, grain size, cell thickness, length of fingers, etc.). The power spectra observed (experimentally and numerically) are not fractal but display small ranges that can be fitted as power law to describe them and compare them.

Moreover, in Figure 8, we can see different power law regimes, fitted by straight curves in this bilogarithmic representation. The exponents (slope) $b1$ and $b2$ and their 95% confidence intervals are obtained after filtering the signal with a low-pass and high-pass filter having 60-kHz cutoff frequency (chosen with respect to the peak frequency), respectively. Next, we calculated the corner frequency where two linear fitting lines having slopes $b1$ and $b2$ coincide. This frequency, in the simulations using air pressure in channels (Figure 8) increases first (until the channel structure stabilizes) and stays at around 100 kHz starting from t = 0.08 s. Depending on the confidence level chosen for the $b1$ and $b2$, the corner frequency may vary from 50 up to 300 kHz. Lamb waves on glass plates have group velocity varying between 2000 and 3000 m/s. We divide the wave velocity by the corner frequency to obtain the range of the characteristic wavelength for this corner frequency (6 cm down to 7 mm), which are in the same range of the width of the channels (15 cm down to 1 cm). In supporting information Figures S14–S16 the figure panels are identical to Figures 8 and 7 but they show more time steps for different pressure contributions. Furthermore, supporting information Figures S17–S25 are provided to show evolution of the mentioned fitting parameters a, b and the corner frequency f_{cr}.

The plate vibrations due to air pressure in the porous medium (Figures 8c and 8d) are weaker but still can be matched with a bi-power law structure that we presented in Figures 8a and 8b. The corner frequency of air vibrations inside the pores is larger than the vibrations inside the empty channels. This is certainly due to the influence of the size of the pores which is much smaller than the size of the empty channels.

Furthermore, the contribution of the solid stress in the cell generated some vibrations. As the perimeter of the compaction zone gets longer we have more fluctuations on the solid stress and, thus, we see more vibrations.

In supporting information Figure S16a, around $t = 0.008$ s we see a very calm structure, which gets very perturbed later (see Figures 8e and 8f) with the effect of fracturation. We can still observe a structure similar to a bi-power law since the structure of the channels is strongly related with the structure of the compaction zone.

If we combine these different contributions, we obtain synthetic vibrations due to total stress variations inside the Hele-Shaw cell. In Figures 7a and 7b, we can fit the power spectra with a bi-power law having a stable corner frequency (around 120 kHz) except at the earliest times like $t = 0.008$ s (shown on the plot at $t = 0.008$ s, supporting information Figure S5), which might be related to the fact that in the very beginning there are not yet any branched patterns of developed channels.

We observe these mentioned evolutions (corner frequency and bi-power law fit) during fracturing in experimental data as seen in Figures 7c and 7d. As we have seen in Figure 5, the structure that we have in both power spectra have similar features. In a logarithmic plot, they both have a quasi linear structure between 4 and 40 kHz followed by a peak at 57 kHz, which is followed by a linear decay toward the higher frequencies. Apart from the similarities, at very low frequencies (lower than 1 kHz) due to the discretization we start to have separation of the two spectra.

By analyzing part by part the different source characteristics in the simulations, we see that the power spectra of air pressure vibrations in the cavity approach to the power law fits. The main source of noise during fracturing is the solid stress, and once the medium stabilizes it is the air vibration.

4.4. Nondimensionalization and Analogy With Liquid-Induced Rock Fracture

For underground rocks, some situations correspond to more deformable layers embedded between layers of less deformable (more competent) rocks (Stanek & Eisner, 2013), with an overpressure on a side by man-made pumps, or by naturally induced overpressure (e.g., due to underground flow leading to rising pore pressure, suddenly exerted on the softer formation after the rupture of a lowly permeable barrier).

The equations of motion for the pore pressure, neglecting the inertia leading to the high-frequency pressure variations, can be written using the previously defined equations (8), (9), (11), and (12), which leads—for the dominant terms—to

$$\rho_0\phi_0 c\frac{\partial P}{\partial t} + \rho_0\nabla\cdot(\phi\mathbf{v_f} + (1-\phi)\mathbf{u}) = 0 \tag{21}$$

and eventually to

$$\frac{\partial P}{\partial t} = D\nabla^2 P - \frac{1}{\phi_0 c}\nabla\cdot\mathbf{u} \tag{22}$$

with $D = \kappa/(\mu\phi_0 c)$. Using a pressure unit $P_0 = 1/(\phi_0 c)$, a length unit L, and a time unit $\tau = L^2/D$ with dimensionless quantities $P' = P/P_0$, $r' = r/L$, and $t' = t/\tau$ this can be formulated as

$$\frac{\partial P'}{\partial t'} = \nabla'^2 P' - \frac{1}{\phi_0 c P_0}\nabla'\cdot\mathbf{u}' \tag{23}$$

that is,

$$\partial_{t'} P' = \nabla'^2 P' - \nabla'\cdot\mathbf{u}'. \tag{24}$$

Or to leading order,

$$\frac{\partial P'}{\partial t'} = \nabla'^2 P' - \left(\frac{\partial\phi}{\partial t'}\right)/(1-\phi). \tag{25}$$

For the solid, the force balance (neglecting inertial terms) can be written as $\nabla\cdot\sigma_s + \nabla P = 0$, which becomes after nondimensionalization by P_0 and L

$$\nabla'\cdot\sigma_s' + \nabla' P' = 0. \tag{26}$$

The rheology of the solid is determined by a yield criterion corresponding to first order to a Mohr Coulomb criterion. Assuming that the sliding occurs essentially at the boundaries between the layer considered and the surrounding formation, this can be written as

$$\sigma_t^s = \mu_C \sigma_n^s + c_0 \tag{27}$$

where σ_t^s is the tangential effective stress along the layer sides, σ_n^s the normal effective stress, μ_C a friction coefficient, and c_0 the cohesion. The rheology of the deforming rock is analogously represented in the laboratory by the rheology of a dense granular material, which can endure shear but cannot significantly reduce its volume—the hard minerals resisting compression, and sliding on each other according to a Coulomb criterion—as in the model of Niebling et al. (2012a) and Niebling et al. (2012b), or in the description of this article where the solid fraction and the normal stress increase when grains are accumulated along empty channels. Channels with a lower grain content have a very large permeability compared to the surrounding material.

In such configuration, the normal load σ_n^s dominates over cohesion c_0 and can be written for grains confined in a layer as

$$\sigma_n^s = \sigma_0 + K\sigma_{xy}^s \tag{28}$$

where σ_0 is the stress prior to deformation, due to the load of the top formation, or the prestress coming from the preparation, and σ_{xy}^s is the stress tensor in the plane of the deformable layer.

The characteristic stress unit is P_0 of order $P_0^{\text{lab}} = 10^5$ Pa for gas at atmospheric pressure, and $P_0^{\text{rock}} = 2.10^{10}$ Pa for water—assuming $\phi^{rock} = 0.1$ for the rock and $c = 5.10^{-10}$ Pa^{-1} for the liquid.

The prestress in the laboratory, responsible for the yield stress, is of order a few times $\rho_s gh$—for example, $P_1 = 10\rho_s gh = 50$ Pa with a layer of $h = 1$-mm thickness, that is, a dimensionless $P_1' = \rho_s gh/P_0^{\text{lab}} = 50/10^5 = 5.10^{-4}$. This is comparable to a situation in large scale with a vertical stress around $P_1 = P_0^{\text{rock}} P_1' = 2.10^{10} \cdot 5.10^{-4} = 1.10^7$ Pa—corresponding to roughly 0.5 km of rock overburden.

The characteristic length L is set by the layer thickness—$L^{\text{lab}} = h = 1$ mm for the current experiments, $L^{\text{rock}} =$ 10 cm to 10 m in large-scale situations.

The pressure diffusion constant is around $D^{\text{rock}} = 0.2$ m^2/s and $D^{\text{lab}} = 5.6 \cdot 10^{-2}$ m^2/s, evaluated as $D = \kappa/(\mu\phi_0 c)$ from the permeability $\kappa^{\text{lab}} = 5 \cdot 10^{-12}$ m^2, air viscosity $\eta^{\text{lab}} = 1.8 \cdot 10^{-5}$ Pa·s, compressibility $c^{\text{lab}} = 1/P_{\text{atm}} = 10^{-5}$ Pa^{-1}, and porosity $\phi_0 = 0.6$, and assuming for the rock, $\kappa^{\text{rock}} = 10^{-14}$ m^2, viscosity $\mu = 10^{-3}$ Pa·s, compressibility $5 \cdot 10^{-10}$ Pa^{-1}, and porosity $\Phi_0 = 0.1$. This corresponds to unit times $\tau^{\text{rock}} = (L^{\text{rock}})^2/D =$ 5 s, and $\tau^{\text{lab}} = 20$ µs, with $L^{\text{rock}} = 1$ m and $L^{\text{lab}} = 1$ mm; that is, the experiments presented in the current manuscript are 50,000 times faster than their large-scale counterpart, and spatial scales observed in these experiments have to be multiplied by 1,000 in analog rock hydrofracture or eruption/injectite dynamics.

Eventually, the pressures imposed here in the lab, from $P_{\text{inj}}^{\text{lab}} = 0$ to 3.10^5 Pa, correspond to a range of $P'^{\text{lab}}_{\text{inj}} = P_{\text{inj}}^{\text{lab}}/P_0^{\text{lab}} = 0$ to 3, and the overpressures corresponding to this are in the range of $P_{\text{inj}}^{\text{rock}} = P_0^{\text{rock}} P'_{\text{inj}} = 0$ to $3{\cdot}10^{10}$ Pa. Deformation triggered by the injection in such system is observed from an injection pressure around $P'_{\text{inj}} = 0.001$, that is, $P_{\text{inj}}^{\text{rock}} = 2 \cdot 10^7$ Pa (Johnsen, Chevalier, et al., 2008). The experiments described in detail in this manuscript would correspond to a very large imposed pressure, around $P'_{\text{inj}} = 1$, and $P_{\text{inj}}^{\text{rock}} = 2 \cdot 10^{10}$ Pa.

5. Conclusion

The evolution of different source contributions in the acoustic emissions are investigated using numerical simulations. The vibrations due to air pressure variations are found to be governing the power spectra. In the beginning ($t < 0.008$ s), the air injection causes large pressure variations in the area empty of grains in the cell and eventually reaches the solid-air interface and pushes the granular medium. This process creates the major contribution in the low-frequency region ($f < 60$ kHz). Afterward, as the grains are getting compacted, the solid stress starts to generate signals having higher amplitude than in the previous time windows. Since the solid stress has a step-like loading due to sudden compaction and sudden stress release (if channeling occurs after compaction), this loading is stimulating all types of frequencies on the glass plate of the Hele-Shaw cell.

Acknowledgments
We would like to thank Alain Steyer and Miloud Talib for the technical support and M. Farin, K. J. Måløy, J. C. Geminard, D. Or, and L. Rivera for discussions during this work. Also, we would like to acknowledge the contributions of the Editor, the Associated Editor, and the reviewers. This project has received funding from the European Union's Seventh Framework Programme for research under grant agreement 316889, from the INSU ALEAS program, from the Universities of Oslo and Strasbourg via a gjesteforsker program, and an IDEX Espoirs award. Moreover, this work was partly supported by the Research Council of Norway through its Centres of Excellence funding scheme, Project 262644 (PoreLab). The Matlab routines and the data set used in this article are provided in https://doi.org/10.5281/zenodo.1079877.

References

Abdelmalak, M. M., Mourgues, R., Galland, O., & Bureau, D. (2012). Fracture mode analysis and related surface deformation during dyke intrusion: Results from 2D experimental modelling. *Earth and Planetary Science Letters*, *359*, 93–105.

Agency, U. E. P. (1994). *Accutech Pneumatic Fracturing Extraction and Hot Gas Injection Phase One: Applications Analysis Report*. Cincinnati, OH: DIANE Publishing Company.

Aki, K., & Richards, P. G. (2002). *Quantitative Seismology* (2nd ed.). Sausalito, CA: University Science Books.

Aochi, H., Poisson, B., Toussaint, R., & Schmittbuhl, J. (2011). Induced seismicity along a fault due to fluid circulation: Conception and application. In *Japan Geoscience Union Meeting 2011, May 2011*. Makuhari, Chiba, Japan.
Benson, P., Vinciguerra, S., Meredith, P., & Young, R. (2008). Laboratory simulation of volcano seismicity. *Science*, *322*(5899), 249–252. https://doi.org/10.1126/science.1161927
Benson, P. M., Vinciguerra, S., Meredith, P. G., & Young, R. P. (2010). Spatio-temporal evolution of volcano seismicity: A laboratory study. *Earth and Planetary Science Letters*, *297*(1), 315–323. https://doi.org/10.1016/j.epsl.2010.06.033
Berryman, J. G. (1983). Random close packing of hard spheres and disks. *Physical Review A*, *27*, 1053–1061. https://doi.org/10.1103/PhysRevA.27.053
Biot, M. A. (1956a). Theory of propagation of elastic waves in a fluid-saturated porous solid. I. Low-frequency range. *The Journal of the acoustical Society of America*, *28*(2), 168–178.
Biot, M. A. (1956b). Theory of propagation of elastic waves in a fluid-saturated porous solid. II. Higher frequency range. *The Journal of the Acoustical Society of America*, *28*(2), 179–191.
Bouchut, F., Fernández-Nieto, E. D., Mangeney, A., & Narbona-Reina, G. (2016). A two-phase two-layer model for fluidized granular flows with dilatancy effects. *Journal of Fluid Mechanics*, *801*, 166–221.
Bracewell, R. (2000). *The Fourier transform and its applications, Electrical Engineering Series*. New York: McGraw Hill.
Carman, P. C. (1937). Fluid flow through granular beds. *Transactions-Institution of Chemical Engineeres*, *15*, 150–166.
Charléty, J., Cuenot, N., Dorbath, L., Dorbath, C., Haessler, H., & Frogneux, M. (2007). Large earthquakes during hydraulic stimulations at the geothermal site of soultz-sous-forêts. *International Journal of Rock Mechanics and Mining Sciences*, *44*(8), 1091–1105. https://doi.org/10.1016/j.ijrmms.2007.06.003
Cornet, F. (2015). *Elements of Crustal Geomechanics*. Cambridge, UK: Cambridge University Press.
Cornet, F., Helm, J., Poitrenaud, H., & Etchecopar, A. (1998). Seismic and aseismic slips induced by large-scale fluid injections, *Seismicity Associated with Mines, Reservoirs and Fluid Injections* (pp. 563–583). New York: Springer.
Cuenot, N., Dorbath, C., & Dorbath, L. (2008). Analysis of the microseismicity induced by fluid injections at the EGS site of soultz-sous-forêts (Alsace, France): Implications for the characterization of the geothermal reservoir properties. *Pure and Applied Geophysics*, *165*(5), 797–828. https://doi.org/10.1007/s00024-008-0335-7
Darcy, H. (1856). *Les Fontaines Publiques De La Ville De Dijon: Exposition Et Application*... Paris, France: Victor Dalmont.
Dorbath, L., Cuenot, N., Genter, A., & Frogneux, M. (2009). Seismic response of the fractured and faulted granite of soultz-sous-forêts (france) to 5 km deep massive water injections. *Geophysical Journal International*, *177*(2), 653–675. https://doi.org/10.1111/j.1365-246X.2009.04030.x
Elkhoury, J. E., Brodsky, E. E., & Agnew, D. C. (2006). Seismic waves increase permeability. *Nature*, *441*(7097), 1135–1138.
Eriksen, J. A., Marks, B., Sandnes, B., & Toussaint, R. (2015). Bubbles breaking the wall: two-dimensional stress and stability analysis. *Physical Review E*, *91*(5), 52204.
Eriksen, F. K., Toussaint, R., Måløy, K. J., & Flekkøy, E. G. (2015). Invasion patterns during two-phase flow in deformable porous media. *Frontiers in Physics*, *3*, 81.
Eriksen, J. A., Toussaint, R., Måløy, K. J., Flekkøy, E., Galland, O., & Sandnes, B. (2018). Pattern formation of frictional fingers in a gravitational potential. *Physical Review Fluids*, *3*(1), 13801.
Eriksen, J. A., Toussaint, R., Måløy, K. J., Flekkøy, E., & Sandnes, B. (2015). Numerical approach to frictional fingers. *Physical Review E*, *92*(3), 32203.
Eriksen, F. K., Toussaint, R., Turquet, A. L., Måløy, K. J., & Flekkøy, E. G. (2017). Pneumatic fractures in confined granular media. *Physical Review E*, *95*, 62901. https://doi.org/10.1103/PhysRevE.95.062901
Eriksen, F. K., Toussaint, R., Turquet, A. L., Måløy, K. J., & Flekkøy, E. G. (2018). Pressure evolution and deformation of confined granular media during pneumatic fracturing. *Physical Review E*, *97*, 12908. https//doi.org/10.1103/PhysRevE.97.012908
Farin, M., Mangeney, A., De Rosny, J., Toussaint, R., Sainte Marie, J., & Shapiro, N. (2016). Experimental validation of theoretical methods to estimate the energy radiated by elastic waves during an impact. *Journal of Sound and Vibration*, *362*, 176–202.
Farquharson, J. I., Heap, M. J., & Baud, P. (2016). Strain-induced permeability increase in volcanic rock. *Geophysical Research Letters*, *43*, 11,603–11,610. https://doi.org/10.1002/2016GL071540
Farquharson, J., Heap, M. J., Varley, N. R., Baud, P., & Reuschlé, T. (2015). Permeability and porosity relationships of edifice-forming andesites: a combined field and laboratory study. *Journal of Volcanology and Geothermal Research*, *297*, 52–68.
Feynman, R. P., Leighton, R. B., & Sands, M. (2011). The Feynman lectures on physics, *Vol. I: The new Millennium edition: Mainly mechanics, radiation, and heat, Basic Books* (Vol. 1). Reading, MA: Addison Wesley Publishing Company Inc.
Flekkøy, E. G., Malthe Sørenssen, A., & Jamtveit, B. (2002). Modeling hydrofracture. *Journal of Geophysical Research*, *107*(B8), 2151.
Galland, O., Holohan, E. P., van Wyk de Vries, B., & Burchardt, S. (2018). Laboratory Modelling of Volcano Plumbing Systems: A Review. In C. Breitkreuz & S. Rocchi (Eds.), *Physical Geology of Shallow Magmatic Systems - Dykes, Sills and Laccoliths* (pp. 147–214). Berlin, Heidelberg: Springer. https://soi.org/10.1007/11157_2015_9
Gao, F., Xie, H., Zhou, F., Ju, Y., Xie, L., Liu, Y., et al. (2014). Pneumatic fracturing method and system for exploiting shale gas. uS Patent App. 14/335,935.
Ghani, I., Koehn, D., Toussaint, R., & Passchier, C. W. (2013). Dynamic development of hydrofracture. *Pure and Applied Geophysics*, *170*(11), 1685–1703.
Ghani, I., Koehn, D., Toussaint, R., & Passchier, C. W. (2015). Dynamics of hydrofracturing and permeability evolution in layered reservoirs. *Frontiers in Physics*, *3*, 67.
Gidaspow, D. (1994). *Multiphase flow and fluidization: Continuum and kinetic theory descriptions*. London, UK: Academic Press.
Goren, L., Aharonov, E., Sparks, D., & Toussaint, R. (2010). Pore pressure evolution in deforming granular material: A general formulation and the infinitely stiff approximation. *Journal of Geophysical Research*, *115*, B09216. https://doi.org/10.1029/2009JB007191
Goren, L., Aharonov, E., Sparks, D., & Toussaint, R. (2011). The mechanical coupling of fluid-filled granular material under shear. *Pure and Applied Geophysics*, *168*(12), 2289–2323. https://doi.org/10.1007/s00024-011-0320-4
Goyder, H., & White, R. (1980). Vibrational power flow from machines into built-up structures, Part I: Introduction and approximate analyses of beam and plate-like foundations. *Journal of Sound and Vibration*, *68*(1), 59–75.
Guyon, E., Hulin, J. P., Petit, L., & De Gennes, P. G. (2001). *Hydrodynamique Physique*. Les Ulis, France: EDP sciences Les Ulis.
Holtzman, R., Szulczewski, M. L., & Juanes, R. (2012). Capillary fracturing in granular media. *Physical review letters*, *108*(26), 264504.
Hurst, A., Scott, A., & Vigorito, M. (2011). Physical characteristics of sand injectites. *Earth-Science Reviews*, *106*(3), 215–246.
Jackson, R. (2000). *The dynamics of fluidized particles*. Princeton University, New Jersey: Cambridge University Press.
Jamtveit, B., Svensen, H., Podladchikov, Y. Y., & Planke, S. (2004). Hydrothermal vent complexes associated with sill intrusions in sedimentary basins. *Physical geology of high-level magmatic systems*, *234*, 233–241.

Janssen, H. (1895). Versuche über getreidedruck in silozellen, Zeitschr. d. *Vereines deutscher Ingenieure*, *39*(35), 1045–1049.
Johnsen, Ø., Chevalier, C., Lindner, A., Toussaint, R., Clément, E., Måløy, K. J., et al. (2008). Decompaction and fluidization of a saturated and confined granular medium by injection of a viscous liquid or gas. *Physical Review E: Statistical, Nonlinear, and Soft Matter Physics*, *78*(5), 51302.
Johnsen, Ø., Toussaint, R., Måløy, K. J., & Flekkøy, E. G. (2006). Pattern formation during air injection into granular materials confined in a circular hele-shaw cell. *Physical Review E: Statistical, Nonlinear, and Soft Matter Physics*, *74*(1), 11301.
Johnsen, Ø., Toussaint, R., Måløy, K., Flekkøy, E., & Schmittbuhl, J. (2008). Coupled air/granular flow in a linear Hele-Shaw cell. *Physical Review E*, *77*(1), 011301. https://doi.org/10.1103/PhysRevE.77.011301
Kausel, E. (2013). Lamb's problem at its simplest. *Proceedings of the Royal Society of London A: Mathematical, Physical and Engineering Sciences*, *469*(2149), 20120462. https://doi.org/10.1098/rspa.2012.0462
Knudsen, H. A., Sandnes, B., Flekkøy, E. G., & Måløy, K. J. (2008). Granular labyrinth structures in confined geometries. *Physical Review E*, *77*(2), 21301.
Kunii, D., & Levenspiel, O. (1991). *Fluidization engineering, Butterworth-Heinemann series in chemical engineering*. Oxford, UK: Butterworth-Heinemann.
Lamb, H. (1904). On the propagation of tremors over the surface of an elastic solid. *Philosophical Transactions of the Royal Society of London. Series A, Containing papers of a mathematical or physical character*, *203*, 1–42.
Lemaire, E., Abdelhaye, Y. O. M., Larue, J., Benoit, R., Levitz, P., & Damme, H. V. (1993). Pattern formation in noncohesive and cohesive granular media. *Fractals*, *1*(04), 968–976.
Levy, H., & Lessman, F. (1961). *Finite Difference Equations*. North Chelmsford, MA: Courier Corporation.
McNamara, S., Flekkøy, E. G., & Måløy, K. J. (2000). Grains and gas flow: Molecular dynamics with hydrodynamic interactions. *Physical Review E*, *61*, 44054. https://doi.org/10.1103/PhysRevE.97.012908
Niebling, M. J., Flekkøy, E. G., Måløy, K. J., & Toussaint, R. (2010a). Mixing of a granular layer falling through a fluid. *Physical Review E: Statistical, Nonlinear, and Soft Matter Physics*, *82*(1), 11301.
Niebling, M. J., Flekkøy, E. G., Måløy, K. J., & Toussaint, R. (2010b). Sedimentation instabilities: Impact of the fluid compressibility and viscosity. *Physical Review E*, *82*, 51302. https://doi.org/10.1103/PhysRevE.82.051302
Niebling, M. J., Toussaint, R., Flekkøy, E. G., & Måløy, K. J. (2012a). Dynamic aerofracture of dense granular packings. *Physical Review E: Statistical, Nonlinear, and Soft Matter Physics*, *86*(6), 61315.
Niebling, M. J., Toussaint, R., Flekkøy, E., & Måløy, K. (2012b). Numerical studies of aerofractures in porous media. *Revista Cubana de Fisica*, *29*(1E), 1E66–1E70.
Oppenheim, A. V. (1999). *Discrete-time signal processing*. Delhi, India: Pearson Education India.
Poiseuille, J. L. M. (1847). *Recherches expérimentales sur le mouvement des liquides de nature différente dans les tubes de très petits diamètres*. Paris: Bachelier.
Royer, D., Morgan, D., & Dieulesaint, E. (1999). *Elastic waves in solids I: Free and guided propagation, advanced texts in physics*. New York: Springer Berlin Heidelberg.
Sandnes, B., Flekkøy, E., Knudsen, H., Måløy, K., & See, H. (2011). Patterns and flow in frictional fluid dynamics. *Nature Communications*, *2*, 288.
Schuring, J. R., Kosson, D. S., Fitzgerald, C. D., & Venkatraman, S. (1996). Pneumatic fracturing and multicomponent injection enhancement of in situ bioremediation. US Patent 5560737.
Scott, G. D. (1961). Packing of spheres. *Nature, 188*, 908–909.
Šílený`, J., Hill, D. P., Eisner, L., & Cornet, F. H. (2009). Non–double-couple mechanisms of microearthquakes induced by hydraulic fracturing. *Journal of Geophysical Research*, *114*, B08307. https://doi.org/10.1029/2008JB005987
Stanek, F., & Eisner, L. (2013). New model explaining inverted source mechanisms of microseismic events induced by hydraulic fracturing. In *SEG Technical Program Expanded Abstracts 2013, Society of Exploration Geophysicists*, (pp. 2201–2205).
Svensen, H., Jamtveit, B., Planke, S., & Chevallier, L. (2006). Structure and evolution of hydrothermal vent complexes in the Karoo basin, South Africa. *Journal of the Geological Society*, *163*(4), 671–682.
Trulsson, M., Andreotti, B., & Claudin, P. (2012). Transition from the viscous to inertial regime in dense suspensions. *Physical Review Letters*, *109*(11), 118305.
Turkaya, S., Toussaint, R., Eriksen, F. K., Lengliné, O., Daniel, G., Flekkøy, E. G., & Måløy, K. J. (2016). Note: Localization based on estimated source energy homogeneity. *Review of Scientific Instruments*, *87*(9), 96101.
Turkaya, S., Toussaint, R., Eriksen, F. K., Zecevic, M., Daniel, G., Flekkøy, E. G., & Måløy, K. J. (2015). Bridging aero-fracture evolution with the characteristics of the acoustic emissions in a porous medium. *Frontiers in Physics*, *3*, 70.
Ugelstad, J., Berge, A., Ellingsen, T., Schmid, R., Nilsen, T.-N., Mørk, P., et al. (1992). Preparation and application of new monosized polymer particles. *Progress in Polymer Science*, *17*(1), 87–161.
Valkó, P., & Economides, M. (1995). *Hydraulic fracture mechanics*. Chichester: Wiley.
Van der Hoef, M., Ye, M., van Sint Annaland, M., Andrews, A., Sundaresan, S., & Kuipers, J. (2006). Multiscale modeling of gas-fluidized beds. *Advances in Chemical Engineering*, *31*, 65–149.
Vass, A., Koehn, D., Toussaint, R., Ghani, I., & Piazolo, S. (2014). The importance of fracture-healing on the deformation of fluid-filled layered systems. *Journal of Structural Geology*, *67*, 94–106.
Vinningland, J. L., Johnsen, Ø., Flekkøy, E. G., Toussaint, R., & Måløy, K. J. (2007a). Granular Rayleigh-Taylor Instability: Experiments and simulations. *Physical Review Letters*, *99*, 048001. https://doi.org/10.1103/PhysRevLett.99.048001
Vinningland, J. L., Johnsen, Ø., Flekkøy, E. G., Toussaint, R., & Måløy, K. J. (2007b). Experiments and simulations of a gravitational granular flow instability. *Physical Review E: Statistical, Nonlinear, and Soft Matter Physics*, *76*(5), 51306.
Vinningland, J. L., Johnsen, Ø., Flekkøy, E. G., Toussaint, R., & Måløy, K. J. (2010). Size invariance of the granular rayleigh-taylor instability. *Physical Review E: Statistical, Nonlinear, and Soft Matter Physics*, *81*(4), 41308.
Vinningland, J. L., Toussaint, R., Niebling, M., Flekkøy, E. G., & Måløy, K. J. (2012). Family-Vicsek scaling of detachment fronts in granular Rayleigh-Taylor instabilities during sedimentating granular/fluid flows. *European Physical Journal: Special Topics*, *204*(1), 27–40.